

**SOLAR POWERED HYDROGEN GENERATION
VIA CARBON-DOPED TiO₂ ANODES**

by

Melissa Day

A thesis submitted to the Faculty of the University of Delaware in partial fulfillment of the requirements for the Honors Bachelor of Chemical Engineering with Distinction.

Spring 2009

Copyright 2009 Melissa Day
All Rights Reserved

**SOLAR POWERED HYDROGEN GENERATION
VIA CARBON-DOPED TiO₂ ANODES**

by

Melissa Day

Approved: _____
S. Ismat Shah, Ph.D.
Professor in charge of thesis on behalf of the Advisory Committee

Approved: _____
Jingguang G. Chen, Ph.D.
Committee member from the Department of Chemical Engineering

Approved: _____
Pei C. Chiu, Ph.D.
Committee member from the Board of Senior Thesis Readers

Approved: _____
Alan Fox, Ph.D.
Director, University Honors Program

ACKNOWLEDGMENTS

I would like to offer thanks and acknowledgement to a few people: Ismat Shah, who has offered me education and opportunities from Crete to the lab; Meghan Schulz, a graduate student who I had the good fortune to work for and whose enthusiasm about life is contagious; Sammy Lin and the rest of the Shah lab; and my friends and family for putting up with my bouts unavailability as a result of lab.

TABLE OF CONTENTS

LIST OF TABLES.....	vi
LIST OF FIGURES	vii
ABSTRACT	ix
Chapter	
1 INTRODUCTION	1
1.1 Main Process	2
1.2 Research Goals	7
2 METHODS.....	8
2.1 Pulsed Laser Deposition	8
2.2 Analysis	11
2.2.1 X-Ray Diffraction.....	11
2.2.2 Ultraviolet-Visible Spectroscopy	12
2.2.3 SEM / EDX	13
2.2.4 PEC Measurements	14
3 CARBON DIOXIDE TRIALS	17
3.1 Rationale.....	17
3.2 Results and Discussion	17
3.2.1 Substrate to Target Distance.....	17
3.2.2 Carbon Doping Efficacy	19

4	METHANE TRIALS	24
4.1	Rationale.....	24
4.2	Results and Discussion.....	25
4.2.1	XRD Results.....	26
4.2.2	SEM Results.....	32
4.2.3	UV-Vis Results.....	33
4.2.4	PEC Cell Results.....	36
5	CONCLUSION	39
	REFERENCES	41
	Cited Works.....	41
	Additional References.....	43

LIST OF TABLES

Table 1.1	Basic structural characteristics of all three TiO ₂ crystal structures.	5
Table 4.1	Film thickness data as obtained by cross-sectional SEM.	32

LIST OF FIGURES

Figure 1.1	Chemical reactions showing the SMR process and CO ₂ evolution.....	2
Figure 1.2	Representation of a photoelectrochemical cell, Bak <i>et al.</i> , 2002.	3
Figure 1.3	Representation of the unit cells for anatase, rutile, and brookite forms of TiO ₂ , respectively from left to right.....	4
Figure 1.4	Solar spectrum with representation of normal TiO ₂ absorption – 5%, UV range – and the potentially attainable visible light region, which constitutes 45% of the solar spectrum.	6
Figure 1.5	Density of states (DOS, arbitrary units) chart from Asahi <i>et al.</i> (2001) that compares the potential efficacy of different types of TiO ₂ dopants.....	6
Figure 2.1	Schematics of a pulsed laser deposition system from Lin <i>et al.</i> (2008).	9
Figure 2.2	Photo of the actual PLD setup in lab.	9
Figure 2.3	Anode configuration for PEC cell tests.	14
Figure 2.4	PEC cell setup with data collection description.	15
Figure 3.1	Analysis of the effects of substrate to target distance on crystallinity.	18
Figure 3.2	UV-vis comparison between pure TiO ₂ and the 1.6 S:T, 100 mtorr CO ₂ sample.....	19
Figure 3.3	Comparison of CO ₂ experiments of varying chamber pressure.	21
Figure 3.4	Labeled XRD pattern of MM061108, the sample deposited under only 25 mtorr CO ₂	21
Figure 3.5	SEM and EDX results for MM060608 (1.6 cm S:T, 100mtorr CO ₂). Top left is 3,500X, top right is 13,000X, bottom is EDX.....	23

Figure 4.1	Comparison of the structure and bond lengths of CH ₄ and CO ₂	24
Figure 4.2	Photograph of the sample batches used in this research. Opacity increases with increase in CH ₄ fraction in the chamber gas.	25
Figure 4.3	XRD results from a CH ₄ batch deposited on ITO glass.	27
Figure 4.4	XRD results from a CH ₄ batch deposited on quartz.	28
Figure 4.5	High-resolution XRD scans of the quartz batch showing the transformation from anatase to rutile with increasing carbon concentration.	29
Figure 4.6	Comparison of rutile c/a and literature data with 0.5% error bars.	30
Figure 4.7	Comparison of grain size data as a function of increasing carbon composition.	31
Figure 4.8	SEM photos taken at 30,000X of four different films to show surface roughness.	33
Figure 4.9	Transmittance data for a CH ₄ batch deposited on quartz.	34
Figure 4.10	Graph of reflectance data after being applied to the Kubelka-Munk theory. Extrapolation lines are shown.	36
Figure 4.11	Selection of voltammetric data for pure TiO ₂ and 70:30, 90:10, and 100:0 samples.	37
Figure 4.12	Selection of IPCE graphs for pure TiO ₂ and 70:30, 90:10, and 100:0 samples.	38

ABSTRACT

Titanium dioxide has excellent qualities as a photocatalyst, yet it only absorbs light in the ultraviolet region. Narrowing the band gap via doping can increase the percentage of solar light it can utilize. When incorporated into a photoelectrochemical cell as an anode, it promotes water splitting, producing oxygen and hydrogen without any harmful byproducts. Pulsed laser deposition has proved useful for tailoring the bandgap of TiO₂ by doping with nitrogen. The same technique is now being utilized to study the effect of carbon doping. Deposition experiments were conducted using a KrF excimer laser ($\lambda = 284$ nm), heating the substrate to 600°C under 100 mTorr total gas mixture pressure, for 20 minutes of a 1.8 J/cm² laser fluence using a 1.6 cm substrate to target distance. Carbon dioxide did not introduce carbon into the TiO₂ lattice due to the overabundance of oxygen. Methane proved to be a more successful carbon precursor. Crystallinity, a shift in preference between anatase and rutile, a red shift in band gap, and changes in thickness and grain size were observed. Visible light activity did not increase, however, due to the formation of intermediate stages in the band gap. This leads to the conclusion that carbon doping by itself is insufficient and co-doping of nitrogen and carbon should be attempted in future research.

Chapter 1

INTRODUCTION

The impact of human beings on the environment has never been acknowledged with as strong a sense of urgency as has been seen in recent years. Air quality and energy sources are now amongst the top issues for the 21st century. Now that particulate matter and automobile emissions are known to contribute to thousands of premature deaths per year¹ and the price of crude oil has fluctuated between \$40 and \$140/barrel² with dangerous economic consequences, it is clear that these sectors are in need of attention. Solar-powered hydrogen generation is one area of research that has the potential to resolve some of these issues. As noted by Back *et al.* (2002), “increasing recognition of the environmental consequences of greenhouse gas emissions can be expected to drive the development of the production of hydrogen from water using solar and other renewable energy resources.” With the aid of a rapidly growing field of current research, the idea of sustainable, emission-free fuel is slowly becoming a possibility.

Using the power of the sun to generate hydrogen by splitting water is one of the cleanest forms of fuel production. The sun is a renewable and sustainable resource, and the process emits only oxygen and hydrogen. At present, however, the cost of this process is significantly higher than competing techniques. One such contender in this field is steam methane reformation (SMR), which is a strong and mature process operating around 70% efficiency – the highest of all the hydrogen production methods.³ Yet a major drawback is the persistent emission of carbon

dioxide, a potent greenhouse gas, via the reaction in Figure 1.1. Some sources claim that SMR produces levels of CO₂ that are double the resulting hydrogen concentration.⁴ As emissions of greenhouse gasses are becoming more heavily restricted under requirements by the Environmental Protection Agency (EPA) and international agreements such as the Kyoto Protocol, it will prove increasingly cost efficient and environmentally sound to develop processes with low to no emissions. Further research into the field of solar-powered hydrogen generation is then both prudent and necessary.

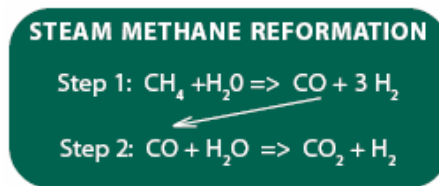


Figure 1.1 Chemical reactions showing the SMR process and CO₂ evolution.³

1.1 Main Process

Any photoelectrochemical, or light-catalyzed water splitting, process follows a general outline for setup and procedure. As shown in Figure 1.2, two electrodes are immersed in an aqueous electrolyte. At least one electrode is a photoelectrode, a semiconductor which is exposed and able to absorb light. Current research has shown that the anode is easier to use in this fashion. Incident photons hit electrons in the semiconductor material and excite them to a state above the band gap of the material. The band gap is located between the filled valence band of electrons and the empty higher energy conduction band. The magnitude of the bandgap

determines how much energy is required to excite the electrons. Excitation creates holes in the base energy bands, which migrate to the anode/electrolyte interface to evolve active oxygen species that react to oxidize water. The electrons go through the external circuit to reduce water at the cathode, producing hydrogen. The reaction proceeds according to the overall equation

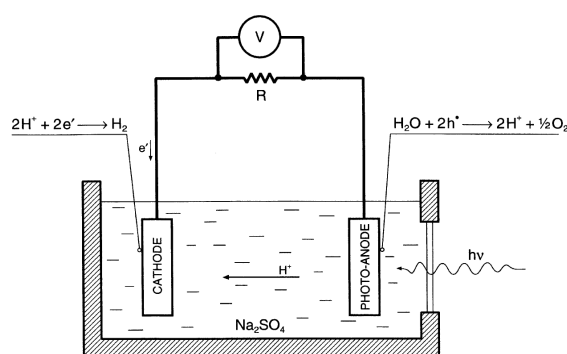


Figure 1.2 Representation of a photoelectrochemical cell, Bak *et al.*, 2002.

An optimal photoanode material must possess specific qualities. Stability and corrosion resistance in electrolytic solutions are necessary for feasible long-term use. The ability to catalyze water decomposition via reduction-oxidation chemistry allows the anode to perform the task at hand. For this purpose, the chemical potential energy must be properly aligned with that of water.⁵ Finally, the material must be able to perform at varied optical wavelengths in order to obtain the maximal absorption of solar energy. This requires adjusting the band gap of the material such that photons of lower energy than UV, such as visible light and IR, can still adequately generate electron-pair holes. The greater the spectrum available, the more photoefficient the

anode will be, and thus the yield of hydrogen will increase. At present, titanium dioxide (TiO_2), strontium titanate, and zinc oxide are the most widely used photoanode materials.

In practice, titanium dioxide (TiO_2) has been the most promising photocatalyst. For example, catalytically active TiO_2 powder will gradually purify a shallow pool of polluted water given enough sunlight.⁶ The material is readily available, established, stable and inexpensive.⁶ Nevertheless, its efficacy is structure dependent. Crystallinity is desired for these applications because it provides a more ordered molecular structure and generally improved photoresponse.

TiO_2 has three common crystalline structures. Anatase, the most photochemically active crystal structure of TiO_2 , has a band gap of 3.2 eV; rutile, a more compact form, has a band gap of 3.0 eV.⁷ Brookite, the rarest of the three, exhibits no photocatalytic ability. The unit cell representations and characteristics of each form are shown in Figure 1.3 and Table 1.1.

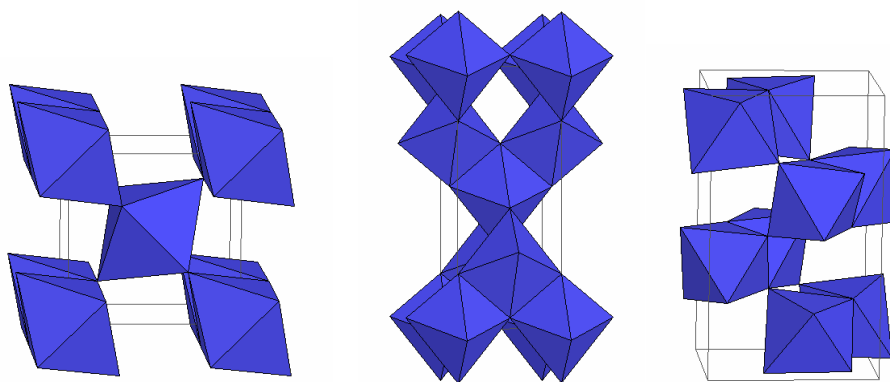


Figure 1.3 Representation of the unit cells for anatase, rutile, and brookite forms of TiO_2 , respectively from left to right.⁸

Table 1.1 Basic structural characteristics of all three TiO₂ crystal structures.⁸

	Rutile	Anatase	Brookite
Crystal System	Tetrahedral	Tetrahedral	Orthogonal
Unit cell, a (Å)	4.5845	3.7842	9.184
b (Å)	-	-	5.447
c (Å)	2.9533	9.5146	5.145
Volume (cm ³)	62.07	136.25	257.38
Molar Volume (cm ³ /mol)	18.693	20.156	19.377
Density (g/cm ³)	4.2743	3.895	4.123

Only the small UV fraction – less than 5% of all solar light – can be absorbed at these band gap sizes. Sensitizing TiO₂ for the much larger visible fraction of incoming light would boost the efficacy of its photoanode behavior, as shown in Figure 1.4. Doping is a common way of modifying the electronic structure. Metallic doping has been shown to produce the desired bandgap reduction, but at the cost of increased recombination and thus lower photoefficiency. Doping of this substance with nonmetals – such as nitrogen, carbon, sulfur, or potassium – has shown some promising results without decreasing carrier lifetime. Asahi *et al.* (2001) determined that nitrogen and carbon in particular produced advantageous electronic structures when incorporated into the TiO₂ lattice. As shown in Figure 1.5, only nitrogen and carbon introduce new density of state (DOS) levels near the edge of the TiO₂ states without also introducing other mid-conductance band states. Having mid-gap states, or states between the valence and conductance bands, may increase the electron hole recombination. Therefore it is desirable to obtain doping as close to the edge as possible. Investigating this possibility with carbon doping thus became of interest.

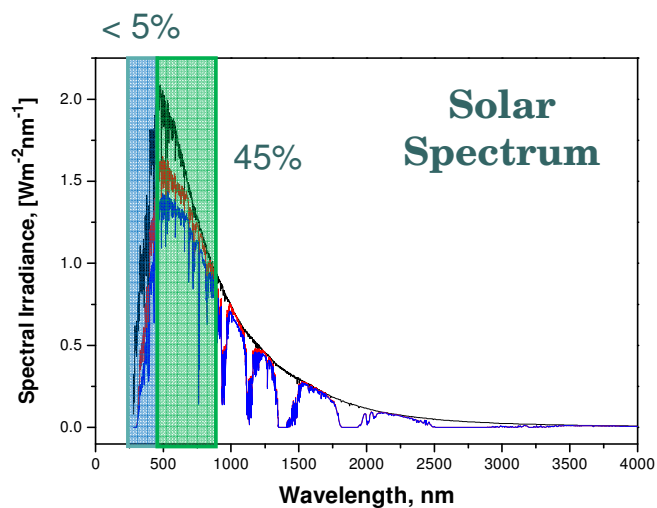


Figure 1.4 Solar spectrum with representation of normal TiO_2 absorption – 5%, UV range – and the potentially attainable visible light region, which constitutes 45% of the solar spectrum.⁹

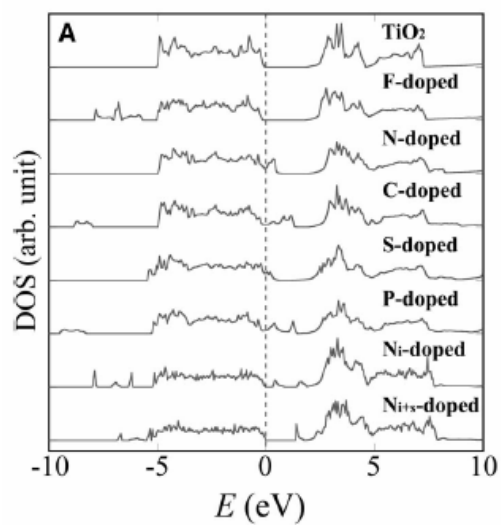


Figure 1.5 Density of states (DOS, arbitrary units) chart from Asahi *et al.* (2001) that compares the potential efficacy of different types of TiO_2 dopants.

1.2 Research Goals

As previously described, using TiO_2 as an anode material has worked in the past, but some improvements are still needed. Research into nitrogen doping of TiO_2 anodes is ongoing in Professor Shah's research group and has met some success.¹⁰ Upon reading reports that carbon-doping can be up to five times more active than nitrogen-doping under visible light irradiation for the purposes of 4-chlorophenol degradation,^{7,11} the team has become interested in looking into adding carbon as well. Similar to the previous nitrogen-doping project and cited works, it is hypothesized that these will give the anodic material a smaller band gap than pure TiO_2 , thus increasing efficacy in the presence of visible light. Based on what is known about the main photoelectrochemical process, three main goals for these experiments have been drafted. These include promoting anatase growth, achieving crystallinity, and obtaining controllable carbon doping that reduces the band gap of TiO_2 . Meeting these objectives would produce a satisfactory product and increase the information available about this material.

Chapter 2

METHODS

2.1 Pulsed Laser Deposition

Of the several TiO₂-doping methods that exist, Pulsed Laser Deposition (PLD) was chosen. The Shah group had used this method previously when testing nitrogen doping¹² and preferred to do the carbon doping in a similar manner for comparison. Figures 2.1 and 2.2 show the basic internal PLD setup and external lab view, respectively. A target and a substrate are inserted before the chamber is pumped down. The target is made of the desired base material, which is pure TiO₂ powder (99.999%, Sigma-Aldrich) for these trials. The powder was compacted into 1” diameter disks; approximately 7.5 grams were used to form about a ¼ inch thick layer of TiO₂. These were then annealed in a tube furnace at 600 °C. The result was ground up, reformed and reannealed for added durability. This builds the strength of the target such that it will not immediately disintegrate upon interaction with the laser. The substrate is a 1” square slide upon which the ablated TiO₂ will be deposited. These slides can be either quartz or indium tin oxide (ITO) coated glass (Delta Technologies Ltd., 4 Ω/□) depending on whether optical or conductive qualities are necessary for analysis of the sample. For most samples, a thin strip called a mask is affixed to the substrate by silver paste. This serves to prevent deposition on this part of the substrate so that the film thickness and deposition rates can be measured.

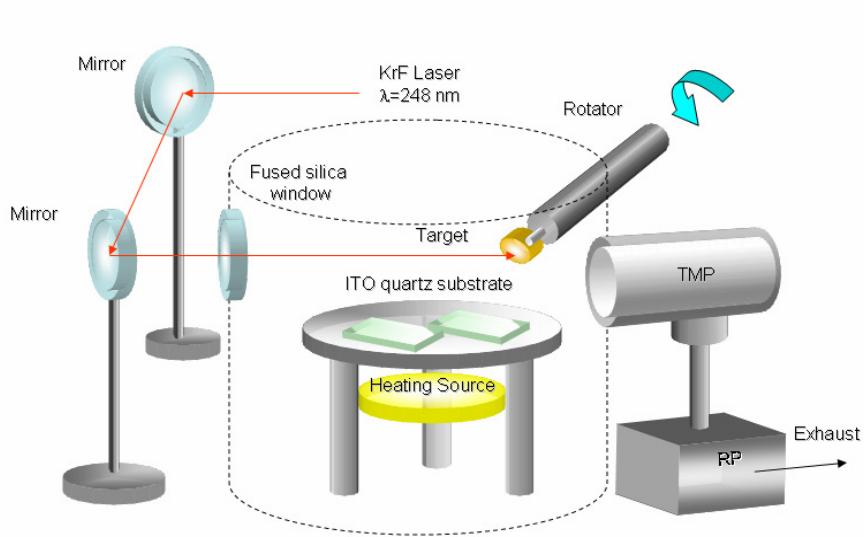


Figure 2.1 Schematics of a pulsed laser deposition system from Lin *et al.*(2008).

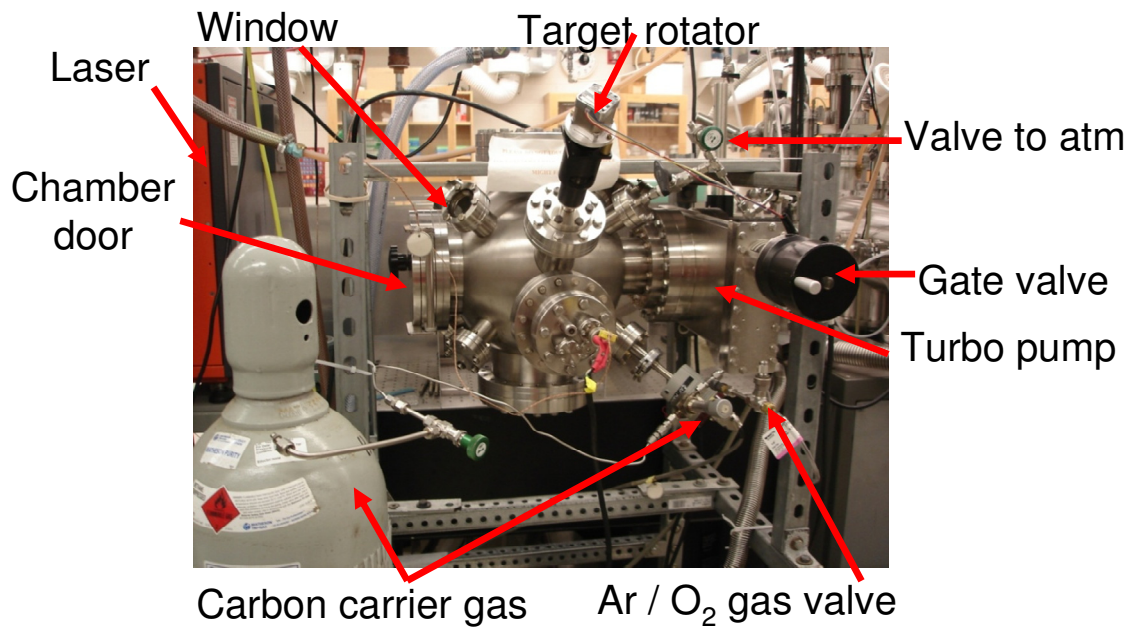


Figure 2.2 Photo of the actual PLD setup in lab.

A KrF gas excimer laser (Lambda Physik LPX 305, $\lambda = 248$ nm) is used, directed into the sample chamber via a series of mirrors. This chamber is under high vacuum – base pressure before gas addition is always under 5×10^{-5} torr – obtained using a rough pump (RP) and turbo mechanical pump (TMP) combination to decrease the interference of air impurities with the laser path and deposition. The laser hits the target, which is rotated at approximately 15 rpm, 45° to the incident laser, to ensure even ablation and deposition. The ablated target material in the form of plasma is ejected into the chamber, which is fed with 100 mtorr of a carbon-containing gas mixture. The goal is for the plume to acquire some carbon as it is deposited on the substrate, which is kept stationary and heated to 600°C via two 500W irradiative halogen lamps. This heating promotes even crystallization as molecules are able to reach a thermodynamically stable configuration. To vary the amount of carbon incorporated into the sample, the ratio to carbon-containing gas to buffer gas (50% Ar, 50% O_2) was changed by the following ratios: 50:50, 60:40, 70:30, 80:20, 90:10, and 100:0, by which samples will be referred in later analysis. Another trial with 100 mtorr of only the Ar / O_2 mixture was used to produce an undoped TiO_2 thin film for comparison. After a certain thickness of the film is achieved – generally $1 - 2 \mu\text{m}$ – the laser and substrate heater are turned off and the sample is left to cool. Once the substrates cool down to room temperature, the system is brought back to atmospheric pressure, the sample is removed for analysis, and the chamber is cleaned if necessary.

Many of the experimental settings were specified and kept consistent throughout the trials. Based on previous Shah Lab research, it was determined that the optimal substrate temperature for crystalline TiO_2 deposition was 600°C . Samples were deposited for 20 minutes at 15 Hz and 400 J, which corresponds to a laser

fluence of 1.8 J/cm^2 . This deposition time yields a satisfactory film thickness as will be later discussed. Above the minimum power density for ablation of the material, a low fluence results in more ordered, stoichiometric crystalline deposition. A higher fluence may cause unsatisfactory crystallinity and larger unincorporated chunks of TiO_2 target material. Finally, the total pressure in the chamber during deposition was kept at 100 mTorr for consistency with previous nitrogen doping trials. These determined that this pressure was optimal for promotion of stoichiometry and crystallinity, as it was not too high that it would introduce too much laser beam interference and not too low so as to induce oxygen vacancies in TiO_2 .

Several parameters required optimization, however, such as the distance between the substrate and the target. A smaller distance ensures that more of the ablated TiO_2 would reach the film and not be lost in the chamber, but this also means that larger chunks of TiO_2 would be present and the sample would not be very uniform. A higher distance would yield a more uniform film but it might be thinner or less robust. Determination of the substrate to target (S:T) distance will be described in Chapter 3. Carbon-containing chamber gas is the second variable in this experiment; Chapter 3 will also show results from the carbon dioxide experiments, and Chapter 4 will detail the methane experiments.

2.2 Analysis

2.2.1 X-Ray Diffraction

X-Ray Diffraction (XRD) is a non-destructive method that can be used to analyze the crystal structure, phase, size, and orientation in samples. Radiation is directed towards the sample at increasing measurements of 2θ , or the angle between

the beam and the diffraction source. The scattered radiation is collected on a detector and shown as a two-dimensional chart of arbitrary “counts” of diffracted radiation versus 2θ . Crystallinity can be determined by the presence of sharp peaks with respect to the background noise, and the phases can be identified by comparing the data to diffraction databases. Grain size can be computed from the full width at half maxima (FWHM) of the peaks using the Scherrer Equation. Within a limit, the sharper the XRD peaks, the larger the crystallite size, according to the equation:

$$\beta_{hkl} = \frac{K\lambda}{L_{hkl} \cos\theta_{hkl}} \quad 2.1$$

In this equation, β is the width of the peak in radians at half of its maximum intensity for a specific phase. K is a constant that varies between 0.89 and 1 depending on the breadth method used, λ is the wavelength of incident x-rays, θ is the center angle of the peak, and L is the crystallite size.

These experiments were performed with a Rigaku D-Max B diffraction system, with a Cu ($K\alpha$) radiation source ($\lambda = 1.5405 \text{ \AA}$) and graphite crystal monochromator. Survey scans of the samples were conducted from $2\theta = 20^\circ - 80^\circ$ with a step size of 0.05° ; specific high-resolution measurements using a step size of 0.002° were also conducted to further investigate TiO_2 lattice parameters. The anatase (101) and rutile (110) reflections were in Region 1, from $2\theta = 24^\circ - 30^\circ$. A(004), A(114), R(101) and R(111) peaks were within Region 2, from $2\theta = 35^\circ - 43^\circ$.

2.2.2 Ultraviolet-Visible Spectroscopy

Ultraviolet-visible (UV-vis) spectroscopy measures photon transmission in the visible, near ultraviolet, and near infrared ranges. The intensity of light passing through a sample is compared to the intensity of light before it passes through the

sample. This ratio is called the transmittance, which is expressed as a percentage (%T). Simple %T measurements do not account for scattered or reflected light, however, so the fraction of incident radiation reflected by a surface (or percent reflectance, %R) is also measured. Change in the band gap of the sample can be approximated by visual inspection of the transmittance or via Kubelka Munk theory. The latter is a more quantitative method that requires more detailed data about the behavior of light on the sample. Light can diffuse, reflect, transmit, or absorb, and %T and %R do not take all of this into account. By using the integrating sphere on the UV-vis and obtaining the diffuse reflectance spectrum (R_∞), however, the light behavior can be better analyzed. The adsorption coefficient can then be calculated via

$$(1 - R_\infty)^2 / 2 * R_\infty = F(R_\infty) \quad 2.213$$

For an indirect semiconductor near its bandgap,

$$F(R_\infty) = B_i(h\nu - E_g)^2 / h\nu \quad 2.314$$

Plotting $h\nu$ against $[F(R_\infty) * h\nu]^{1/2}$ will thus enable determination of E_g , or the band gap energy.

Data for this experiment was collected over 200 – 800 nm using a double-beam Lambda 35 Perkin-Elmer UV-Vis spectrophotometer with an integrating sphere.

2.2.3 SEM / EDX

Scanning electron microscopy (SEM) images the surface of a sample via a high-energy electron beam. Sample atoms interact with the beam of electrons and produce secondary electrons that are used to determine surface topography and composition. It is also possible to determine the thickness of the deposition layer. Energy Dispersive X-ray (EDX) spectroscopy is paired with the available SEM

equipment, and the x-ray energy signals are processed to give atomic structure and composition data. The surface and cross-sectional images in this report came from a JEOL scanning electron microscope, model JSM 7400F. The working distance was kept between 7.2 and 7.4 mm and accelerating voltage was 2-3 kV.

2.2.4 PEC Measurements

As previously explained, a photoelectrochemical (PEC) cell consists of a photoanode and a cathode immersed in an electrolyte. Electrical energy is generated from light and used to split water into H_2 and O_2 . Sample slides from the conductive ITO batch were layered according to Figure 2.3. The thin film was deposited on purchased ITO layered glass with mask affixed to the sample during deposition. After deposition, the mask was removed and a copper wire was silver pasted to the ITO contact area so the sample was connected with the voltammetric system. In the last preparation step, an electrical tape insulating mask was added to ensure that a standardized area of each sample was exposed to the light and electrolytic solution. Finally, the sides were sealed with epoxy and the unit was ready to be tested.

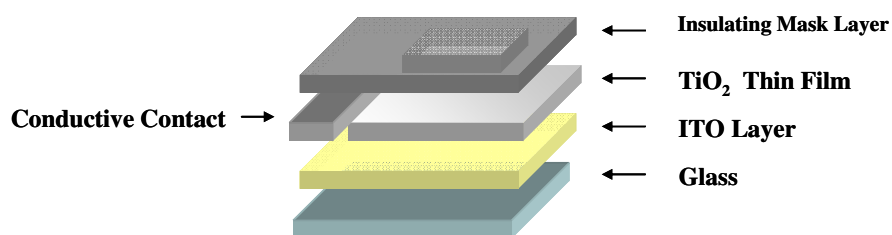


Figure 2.3 Anode configuration for PEC cell tests.

Trials were performed by placing the sample slides into a custom made Teflon PEC cell, using a highly crystalline fused silica window so as to minimize interference of the window with the incoming light. The cell is connected to a potentiostat, where the voltage is varied and current is measured; this setup is shown in Figure 2.4. A lamp shines light of a variable wavelength – starting at 260 nm and increasing up to 700 nm by increments of 20 nm – on the sample for approximately 20 seconds. This series of wavelengths was conducted five times for each sample, for voltages of 0.00, 0.25, 0.50, 0.75, and 1.00 V. The photocurrent transmitted through the sample for each wavelength at each voltage was recorded.

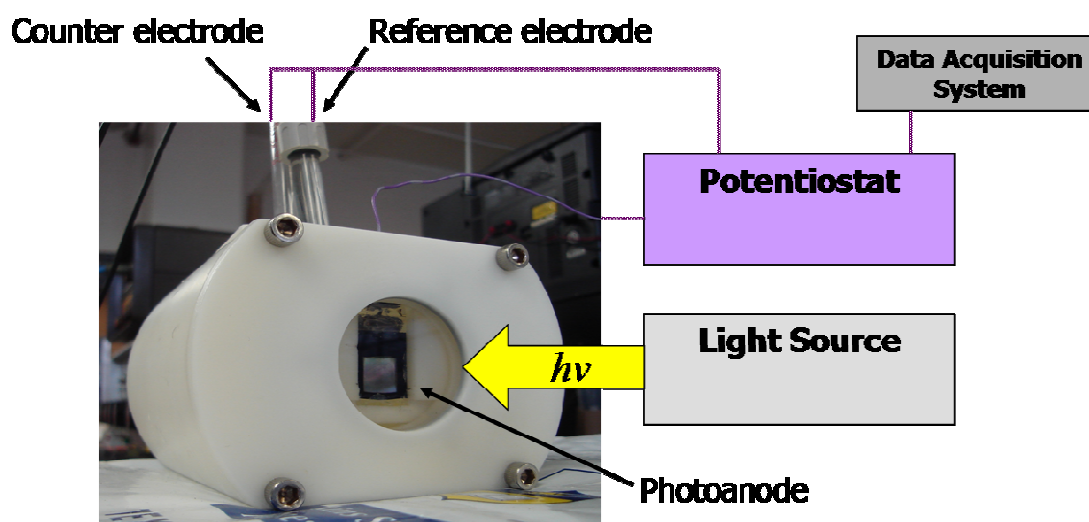


Figure 2.4 PEC cell setup with data collection description.

The photocurrent data was used to evaluate the efficiency of the sample at each wavelength by means of incident photon-to-current conversion efficiency (IPCE). The issue with voltammetry is that it only records the current, which is dependent on

power, which depends on the lamp responsible for the radiation. Whether the lamp is completely warmed up or working exactly the same way each time a measurement is made is not certain, however. To remedy this and produce a more rigorous evaluation of quantum efficiency, IPCE compares the ratio of photoelectrons generated to the total number of incident photons at a given wavelength. This is calibrated to the incident power of the photons, and can be calculated via equation 2.4.

$$IPCE = \frac{j_{photo} N_A hc}{\lambda PF} \quad 2.4^{15}$$

In this equation, j_{photo} is the photocurrent density in A/cm^2 , N_A is Avogadro's number, h is Planck's constant, c the speed of light, wavelength λ is in m, P the incident power in W/cm^2 , and F is the Faraday constant.

Chapter 3

CARBON DIOXIDE TRIALS

3.1 Rationale

Literature sources incited a TiO₂ carbon-doping project and similarly directed the carbon precursor choice. Once carbon was chosen based on the Asahi density of states evaluation, papers involving carbon doping were scrutinized. Park *et al.* (2006)¹⁶ annealed their samples under a controlled carbon monoxide gas flow and successfully produced photoelectrolytic samples. The safety precautions for CO use on campus, however, required a complex and costly new setup. It was also found that Khan *et al.* (2002)¹⁷ had used a gas mixture including CO₂ in flame pyrolysis to produce promising samples; Enache *et al.* (2004)¹⁸ carried out spray pyrolysis in a CO₂/O₂ atmosphere as well. Although the PLD process is not incredibly similar to pyrolysis, it was decided to try CO₂ as the carbon carrier gas for our first trials.

3.2 Results and Discussion

3.2.1 Substrate to Target Distance

After the first few samples were analyzed the substrate to target (S:T) distance became a fixed setting. Shown in Figure 3.1 are the XRD results for three samples run in 100 mtorr CO₂ at varying S:T distance. Lack of peaks in the 5 and 2.4 cm data sets means that those samples were amorphous, as could be determined from

XRD. The first two samples, then, were too far away from the TiO_2 source; the deposition rate at the substrate was very low, and the ablated particles did not crystallize well. The 1.6 cm sample, however, showed clear peaks corresponding to anatase TiO_2 . Decreasing the S:T even further was deemed unnecessary, because although going closer to the target could possibly encourage stronger crystallinity, the uniformity of the sample would decrease further and make analysis difficult. Therefore a S:T distance of approximately 1.6 cm was ideal for crystalline growth and this setting was used for every trial thereafter.

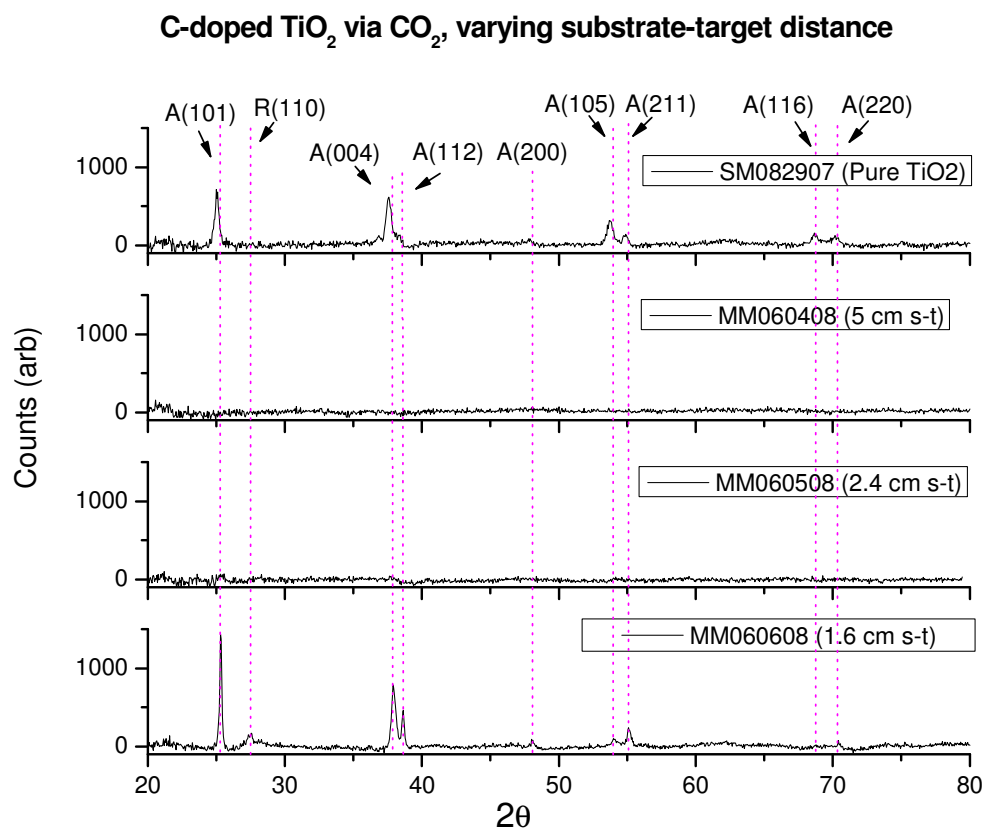


Figure 3.1 Analysis of the effects of substrate to target distance on crystallinity.

3.2.2 Carbon Doping Efficacy

The data seemed promising, but when compared to pure TiO₂ data there was very little carbon-influenced shift in the bandgap. Nothing in the XRD data suggested a carbon related phase, so UV-vis analysis was conducted. As shown in Figure 3.2, it was found that the 1.6 cm S:T sample exhibited an edge in transmittance at very nearly the same wavelength position. This intones that the band gap was not reduced in any significant way, and so relatively little carbon is present in the lattice as a substitutional impurity. This was corroborated visually, in that even though the sample had been deposited in a CO₂-only atmosphere, it did not change its appearance as would be expected for a carbon-doped sample.

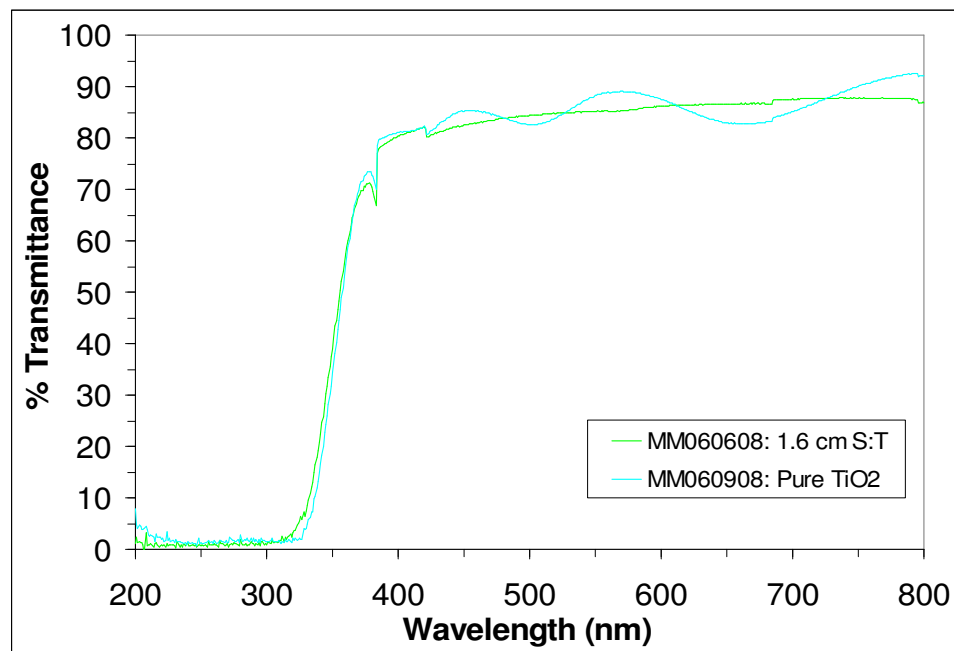


Figure 3.2 UV-vis comparison between pure TiO₂ and the 1.6 S:T, 100 mtorr CO₂ sample.

Different experiments were thus necessary to fully test the abilities of CO₂ as a carbon carrier. Contrary to the suggested 100 mtorr total pressure for the chamber, 25 mtorr CO₂ was attempted to see how carbon incorporation changes with pressure. Depositing in a vacuum and introducing CO₂ during a later annealing period was also tried. Neither yielded satisfactory results, as can be seen in Figure 3.3. The annealed sample showed very little crystallinity and therefore was not a useful film. The lower-pressure CO₂ trial produced a very dark film, which is not beneficial for transmittance, but it did attain crystallinity. Identification of XRD peaks in the sample in Figure 3.4, however, shows predominantly rutile formation with a few peaks resulting from unusual combinations of Ti and O (not TiO₂ but TiO, TiO₃ or otherwise). The presence of phases other than anatase indicates that it would not be an optimal photocatalyst.

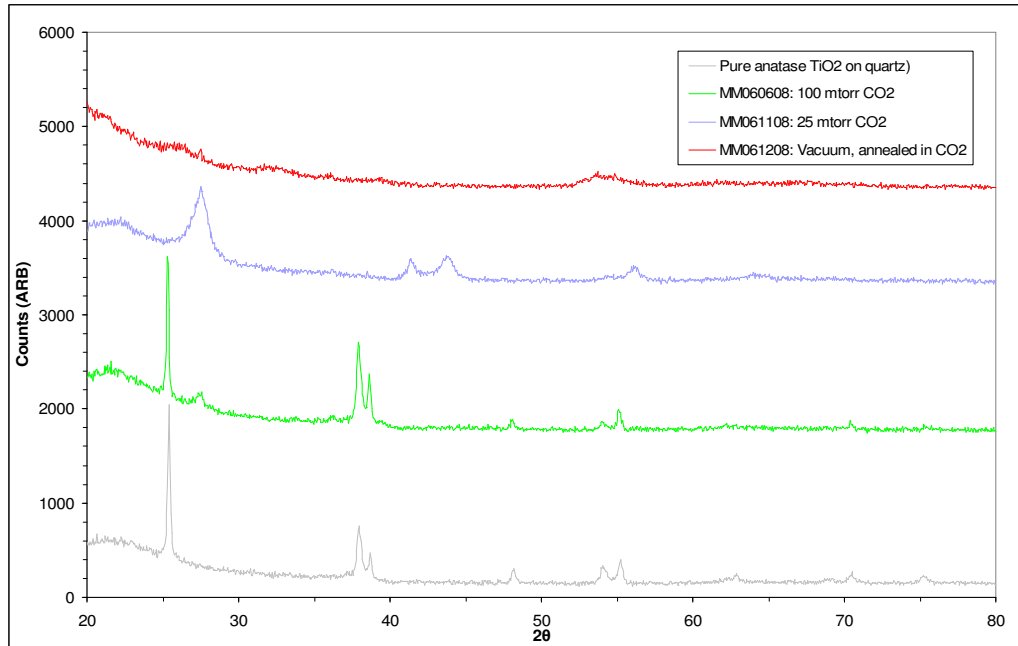


Figure 3.3 Comparison of CO₂ experiments of varying chamber pressure.

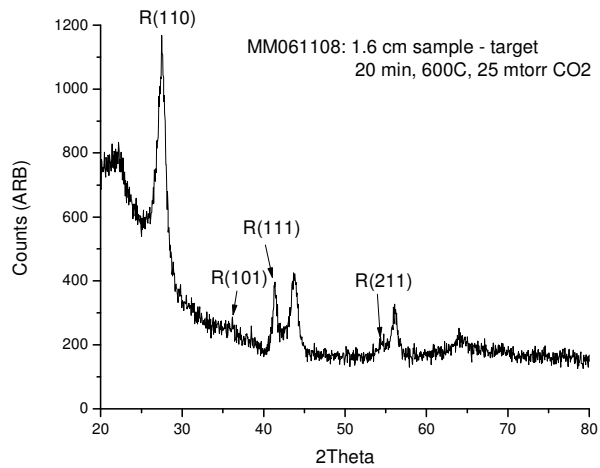


Figure 3.4 Labeled XRD pattern of MM061108, the sample deposited under only 25 mtorr CO₂.

Finally, SEM was used to verify the sample morphology and also to attempt to identify carbon. MM060608, the first crystalline TiO₂ sample, was used. The chunks seen on surface in Figure 3.5 were verified to contain only titanium and oxygen, likely directly from the target. The presence of these chunks is typical in PLD deposition. As shown in the EDX spectrum, the surface had TiO₂ elements and silicon from the quartz substrate. Carbon was very difficult to identify, however, since it is very far left in the spectrum (low keV) and is close in proximity to the very prevalent oxygen and titanium peaks. Carbon is prevalent in many samples due to its abundance in global systems, not just those for which it has been deliberately introduced, and this makes it hard to distinguish. Surface adsorption, therefore, is not particularly useful in identifying carbon content, but it does at least give confirmation of the TiO₂ deposition.

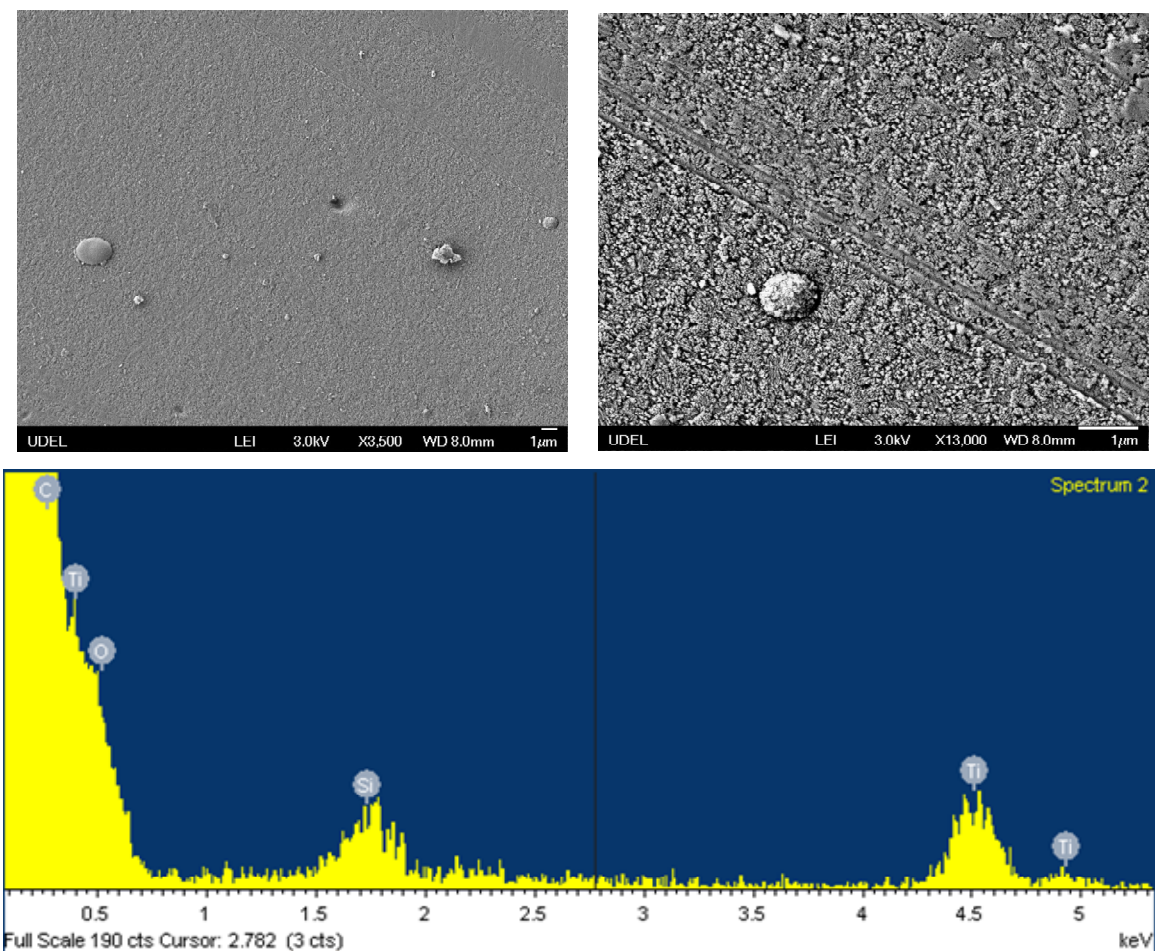


Figure 3.5 SEM and EDX results for MM060608 (1.6 cm S:T, 100mtorr CO₂). Top left is 3,500X, top right is 13,000X, bottom is EDX.

Chapter 4

METHANE TRIALS

4.1 Rationale

Given the lack of success of the CO₂ trials, the decision was made to switch to CH₄ as a carbon carrier. This has more carbon by weight and less oxygen inflow. Lack of carbon insertion in the TiO₂ lattice was attributed to some extent by the preferential binding of oxygen instead, which is abundant in CO₂. Using CH₄ and using a separate 50:50 mix of Ar/O₂ to control the oxygen presence was determined to be a better setup. In addition, although the C-H bond length is shorter than that of C=O (see Figure 4.1), it is not a double bond. The bond energy for CO₂ is about 690 kJ/mol whereas that of CH₄ is about 420 kJ/mol.¹⁹ This lower bond energy of CH₄ would make it easier to introduce into the TiO₂ lattice. As previously discussed, methane is also already part of the current hydrogen production system, which has been highly successful.

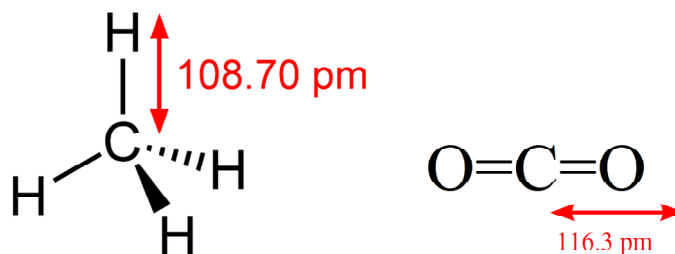


Figure 4.1 Comparison of the structure and bond lengths of CH₄ and CO₂.

4.2 Results and Discussion

Parameters were held the same as previously determined – 600°C, 20 minute ablation, 1.6 S:T distance, and 100 mtorr total pressure. The distribution of the 100 mtorr in the chamber was to be varied by 50-50, 60-40, 70-30, 80-20, 90-10 and 100-0 CH₄ to the Ar/O₂ mix. This was done to control the ratio of carbon and oxygen in the chamber, and the fact that carbon content can be easily varied via gas pressure is one of the advantages of using the PLD. Unlike the CO₂ samples, these emerged different to the naked eye. Whereas the pure TiO₂ and previous trials had resulted in films that were nearly transparent, the methane-doped samples were dark where the laser plume had been most concentrated. The color also became more opaque with increasing methane concentration, showing their absorption in the visible light region. This was more promising, considering that dark gray is characteristic of carbon deposition, and it could be said that we already knew the samples were absorbing some visible light because they had darkened. This effect is shown in Figure 4.2.

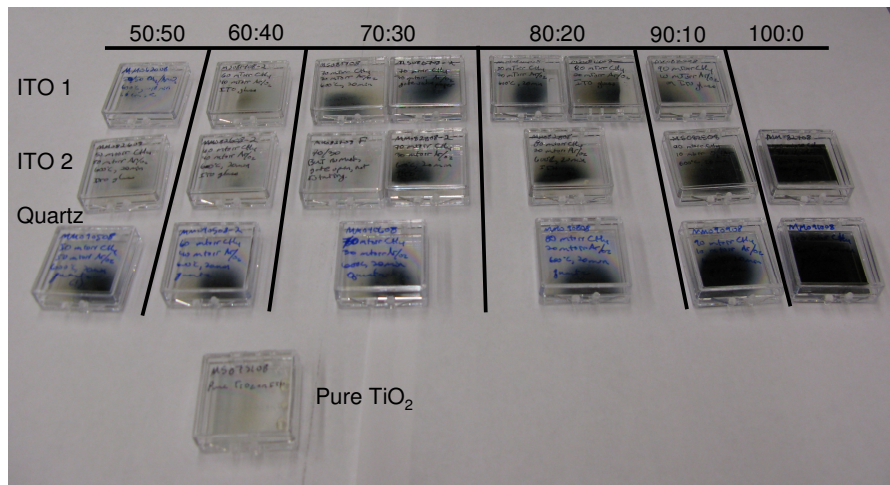


Figure 4.2 Photograph of the sample batches used in this research. Opacity increases with increase in CH₄ fraction in the chamber gas.

Due to the success of the first batch, complete batches were run on both Indium-Tin-Oxide (ITO) coated glass and quartz substrate slides. The ITO slides were intended for the PEC cell and SEM measurements, as for those methods a conductive surface is necessary. TiO_2 films are not conductive ordinarily, so depositing on a surface that is already conductive is the solution. ITO films were also used in XRD analysis, although the additional ITO coating adds to the crystalline peaks in the pattern so care must be taken when investigating the data. The quartz slides were uncoated and used for XRD and UV-vis measurements as it offers less base interference.

4.2.1 XRD Results

The XRD results show a definite change within batches. Figures 4.3 and 4.4 show the initial data for both ITO and quartz batches, and it can be observed that there are variations between runs. A clearer picture is represented by Figure 4.5, however, showing the most interesting part of the results analysis so far.

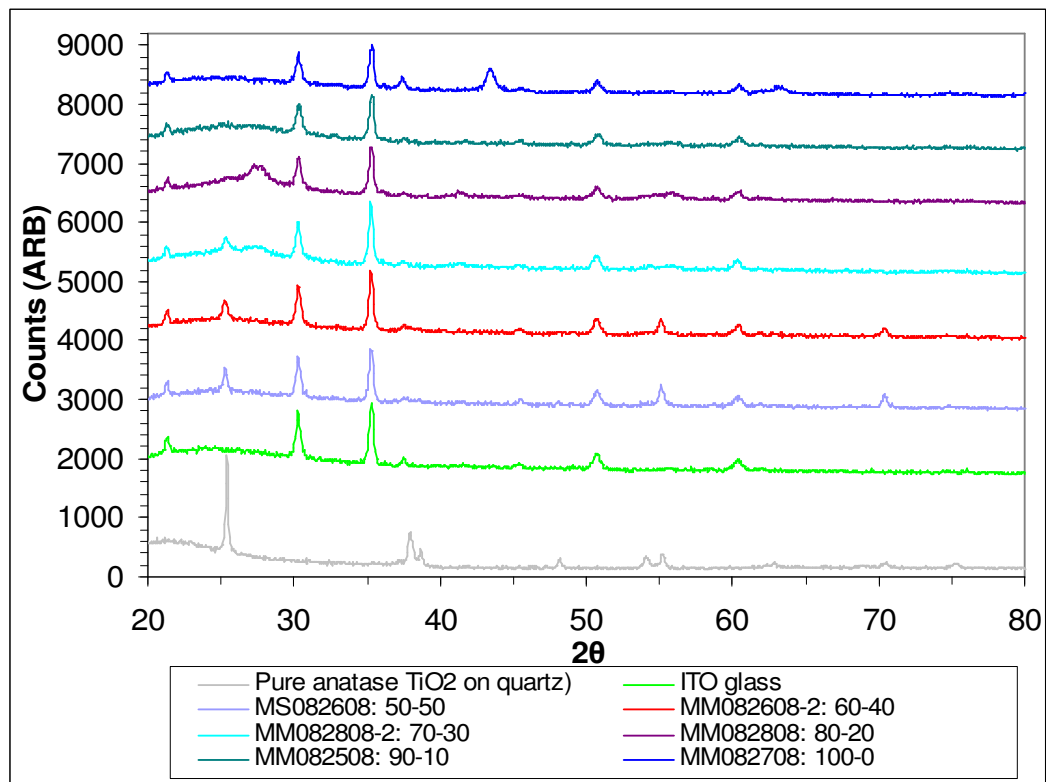


Figure 4.3 XRD results from a CH₄ batch deposited on ITO glass.

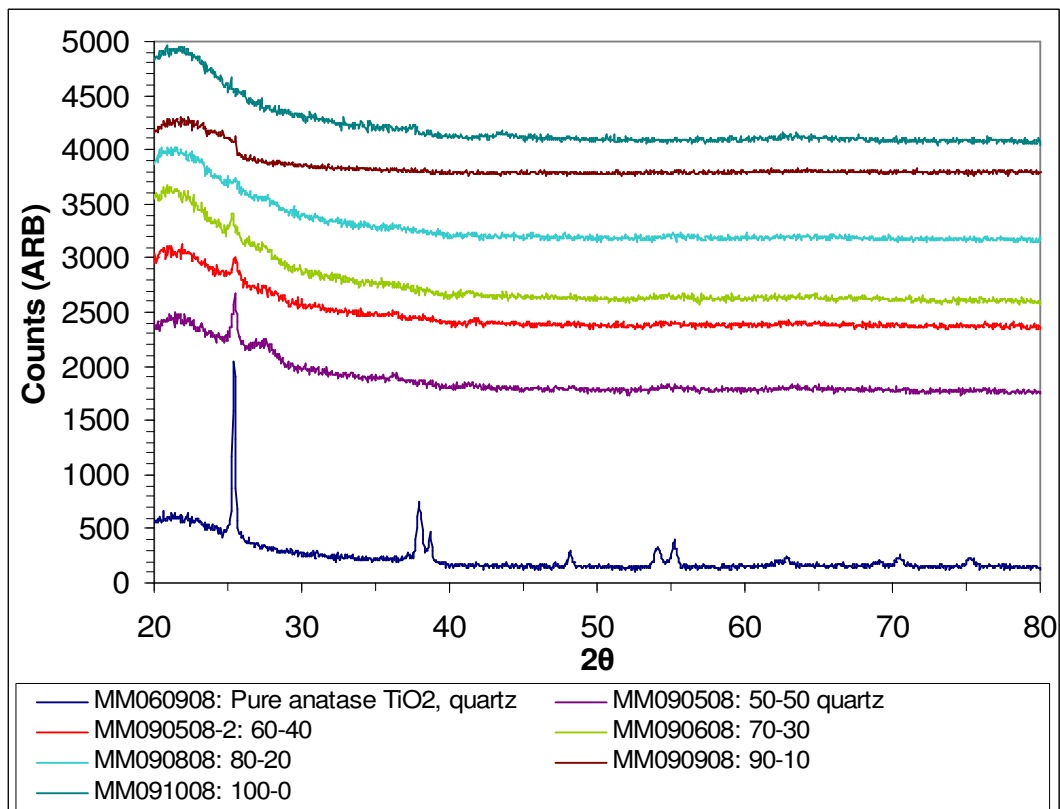


Figure 4.4 XRD results from a CH₄ batch deposited on quartz.

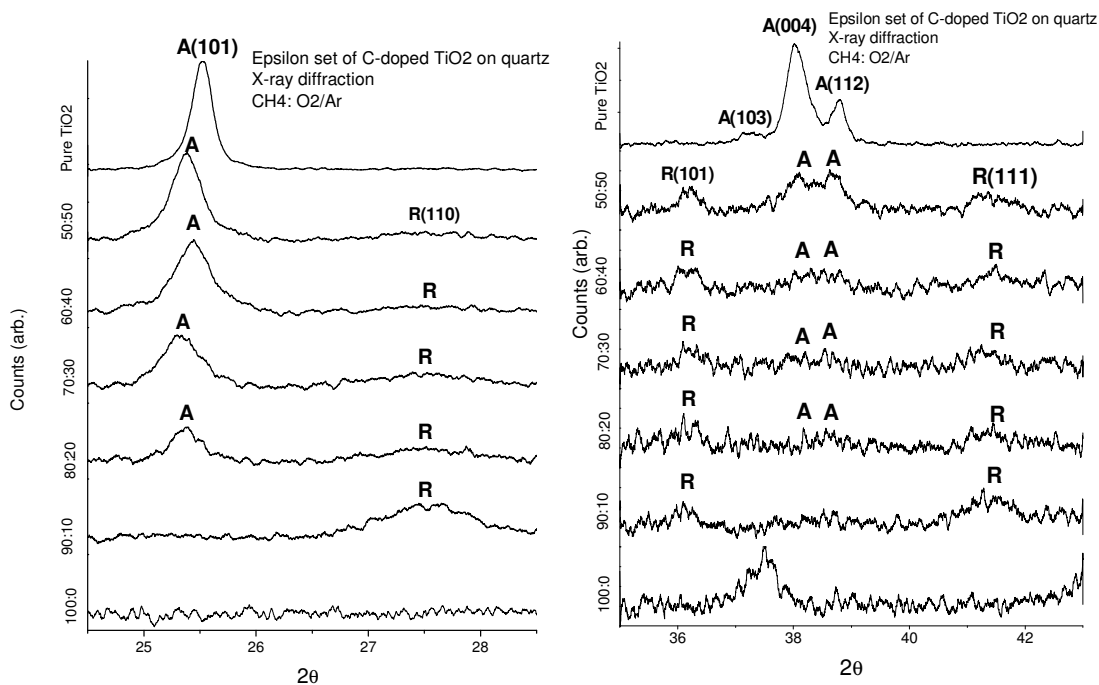


Figure 4.5 High-resolution XRD scans of the quartz batch showing the transformation from anatase to rutile with increasing carbon concentration.

The anatase to rutile peak shift with increasing carbon concentration is most likely a result of carbon doping. As more carbon is interstitially inserted into the anatase lattice, it was thought that the bond lengths would strain to accommodate the different size and the crystal structure gradually changes from anatase, the unit cell of which has a larger c/a , to rutile. When Bragg diffraction theory was used in to determine the c/a , however, Figure 4.6 was the result. The dotted line in the middle is the literature value for the c/a ratio in TiO_2 , with error bars to show 0.5% deviation from this value. All of the calculated rutile c/a is within this ratio, and so it cannot be said that the bond lengths are actually shifting in the way theorized.

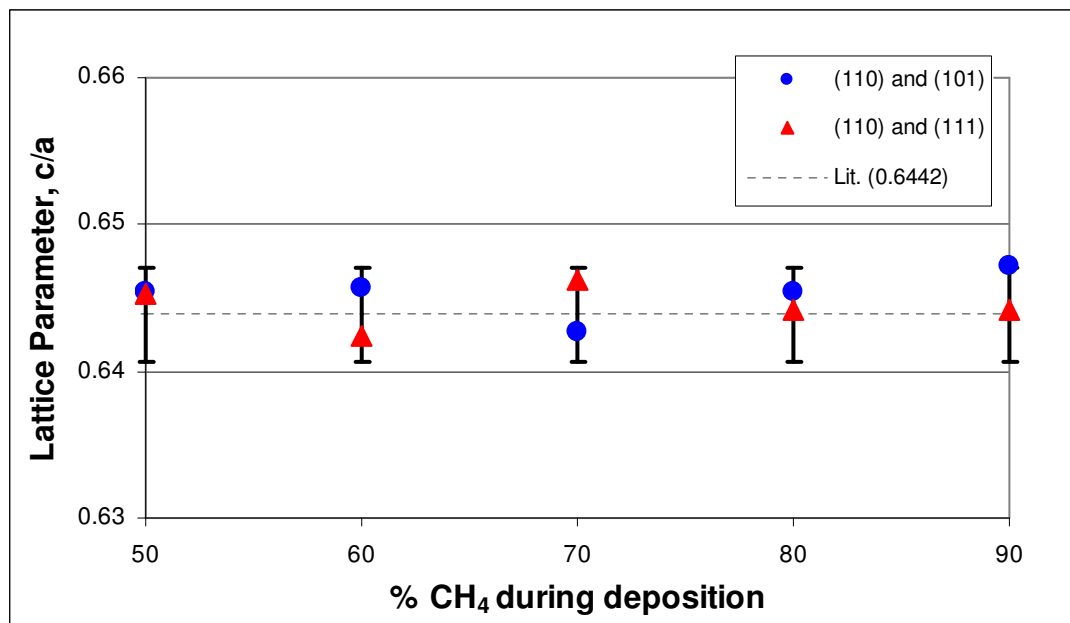


Figure 4.6 Comparison of rutile c/a and literature data with 0.5% error bars.

This phenomenon also has been observed in previous nitrogen doping trials, however, so further investigation of the past data and a literature search could be of interest to more explicitly determine what is occurring. In any case, the fact that crystallinity is shifting seems to be a good indicator of carbon presence, even if whatever is going on is not stretching the lattice.

The high-resolution XRD scans were also used to compute the polycrystalline grain size of the TiO₂ films. Identical Scherrer formula calculations were performed for six different (hkl) crystal orientation reflections, as have been labeled in prior XRD scans. Two anatase and two rutile peaks for each sample were evaluated and the average between the four values was taken for the overall grain size trend. The results in Figure 4.7 show decreasing grain size with carbon deposition. This also seems to support definitive carbon content.

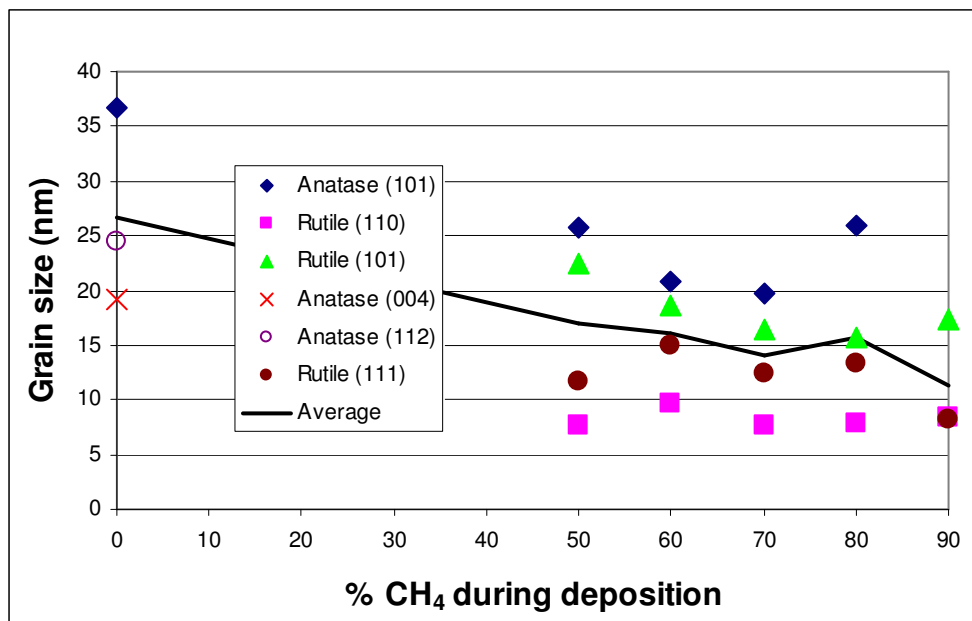


Figure 4.7 Comparison of grain size data as a function of increasing carbon composition.

The grain size data appear to contradict that of the anatase to rutile transformation. In general, nanoparticles tend to have anatase structure because the surface energy induces metastable phase formation. Even smaller particles, then, would be expected to crystallize as anatase as well. In the presence of an impurity such as carbon, however, this tendency might be suppressed. The impurities could result in a higher nucleation density such that diffusion, rather than surface energy, is the dominating criterion for phase stability. Pairing the XRD peaks with the grain size therefore leads to one possible explanation for the anatase to rutile transformation.

4.2.2 SEM Results

Film thickness was measured when cross-sectional SEM was conducted. The results shown in Table 4.1 were obtained from the quartz batch. The average film thickness was approximately 1.4 microns, which equates to 0.08 nm per laser pulse. Also useful is the standard deviation, which shows the large degree to which PLD film thicknesses can vary. Although the procedure remains exactly the same, consistency between films and batches will be affected by this phenomenon. Examples of surface unevenness are shown in Figure 4.8; much of this is attributed to the violent nature of the ablation process as previously explained. It is also observed that the deposition rate decreases with increasing carbon concentration, presumably due to the interference of the ablated flux with the chamber gases. This is in accordance with the grain size reduction discussed earlier, suggesting that carbon content leads to slightly decreased crystallinity. The reduction in grain size is further illustrated in the SEM photographs as well.

Table 4.1 Film thickness data as obtained by cross-sectional SEM.

Sample	Data (μm)				Average (μm)	STD (μm)	nm/sec	nm/pulse
Pure	1.7	1.8	2.9	2.4	2.200	0.560	1.833	0.122
50:50	1.47	1.3	1.8		1.523	0.254	1.269	0.085
80:20	1.031	1.059	1.05		1.047	0.014	0.872	0.058
100:0	0.701	0.722	0.71		0.710	0.011	0.592	0.039
				Average	1.370	0.210	1.142	0.076

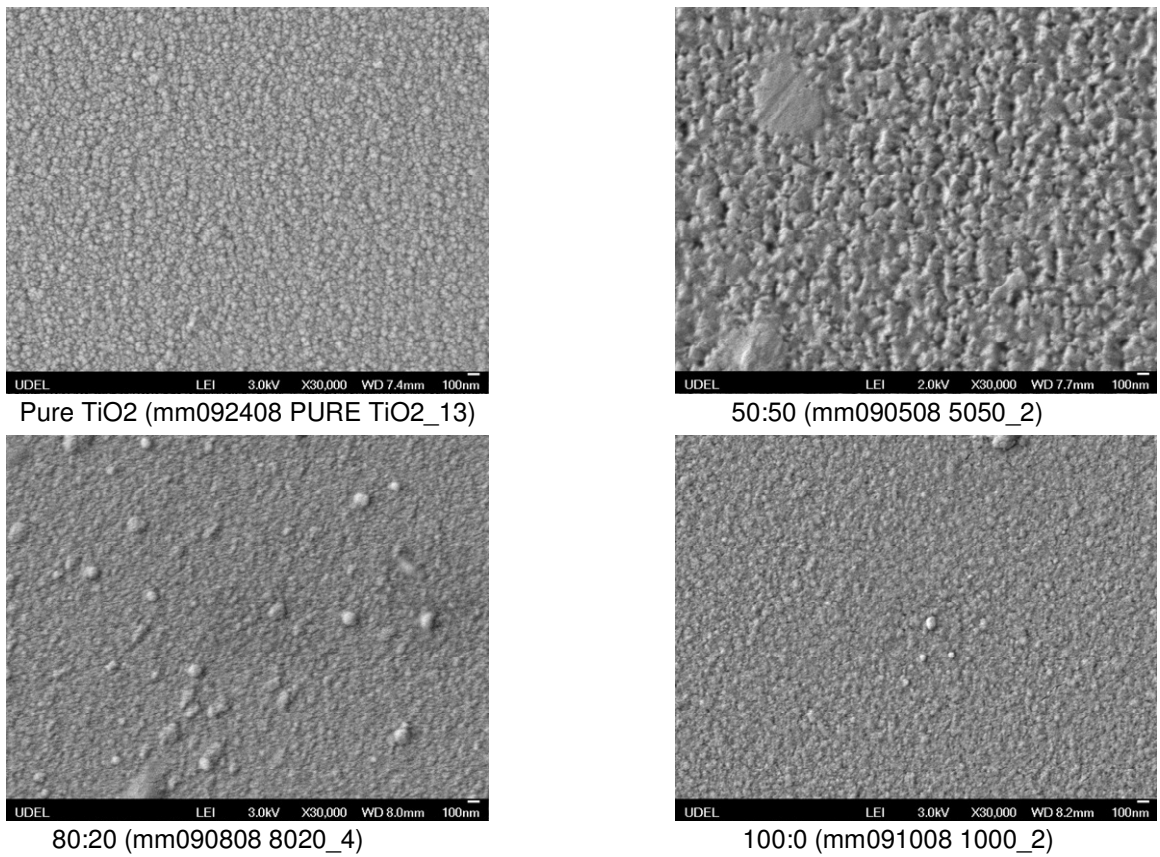


Figure 4.8 SEM photos taken at 30,000X of four different films to show surface roughness.

4.2.3 UV-Vis Results

Basic transmittance results for the batch deposited on ITO glass are shown in Figure 4.9. It is speculated that the transmittance dips in the 500-800 nm region due to intermediate band gap formation. This means the carbon states are not flush with that of the TiO_2 edge. More significant are the drops in transmittance around 350-380 nm, however. The dotted lines denote the band gaps of anatase and rutile, which show

approximately where the transmittance should start to drop. For the samples with lower carbon concentration, the transmittance edges are relatively close between films, potentially indicating that the band gap was not augmented very much. The higher carbon concentration films, as shown in the graph inset, appear to drop earlier, indicating that their band gaps have been altered. UV-vis is more of a qualitative procedure, however, so specific band gap shifts are difficult to determine and transmittance data by itself is not conclusive evidence. It is a promising suggestion, however. It should be noted that the 100:0 trial was completely opaque and thus has no transmittance.

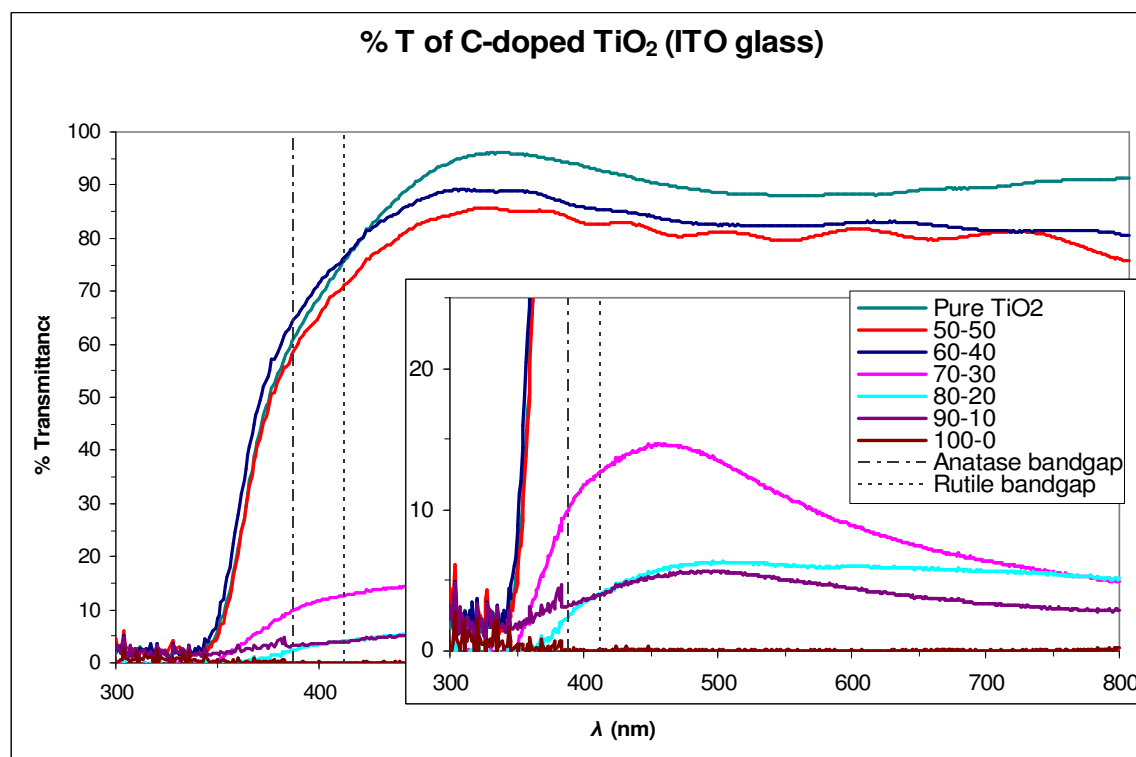


Figure 4.9 Transmittance data for a CH₄ batch deposited on quartz.

In an effort to more accurately determine the band gap of each of the samples, the Kubelka-Munk theory was employed on the quartz batch. As seen in Figure 4.10, extrapolation of the edge of the curves seems to suggest a red shift, towards the visible light region, with increasing carbon concentration. The 50:50 and 60:40 trials show no significant change in bandgap as compared to the pure sample, although they appear to have band gaps of 3.4 eV instead of the theoretical value of 3.2 eV for anatase. In any case, 70:30 and 80:20 are shifted to the right, with 3.2 and 2.85 eV respectively. 90:10 and 100:0 were not included in this figure as the data did not produce meaningful results. The growing opacity of the samples with carbon concentration interfered with the diffuse reflectance data, which also explains why the 70:30 and 80:20 curves never return to the baseline.

These results are not as successful as those of the nitrogen trials but they do show some change in the band gap as a result of carbon doping. This is reinforced by the x-ray photoelectron spectroscopy (XPS) data analyzed by another Shah group member that found defect states above the valence band of TiO_2 . Therefore carbon is depositing in the film and adding its density of states into the band gap. Whether this increased the efficiency of the cells or not is discussed in the next section.

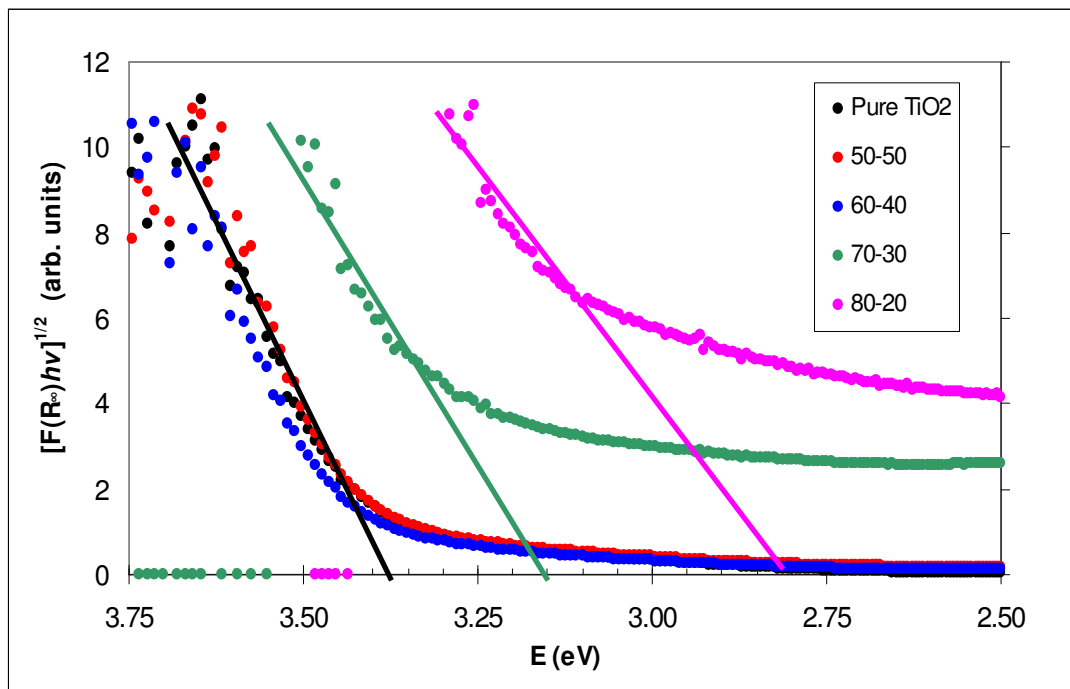


Figure 4.10 Graph of reflectance data after being applied to the Kubelka-Munk theory. Extrapolation lines are shown.

4.2.4 PEC Cell Results

The photocurrent response of samples under UV light (300 nm) and visible light (460 nm) as a result of the voltammetric experiments is shown in Figure 4.11. The 70:30, 90:10, and 100:0 graphs were chosen for a cohesive and non-repetitive representation of film behavior; lower concentrations were excluded based on measurement errors and the 80:20 and 90:10 graphs were effectively identical. It can be seen that the response under UV decreases with increasing carbon content. This was expected, as it was also observed in the nitrogen trials. Contrary to the nitrogen trials, however, the response to visible light stays about the same with increasing carbon concentration. The voltammetry studies involve increasing the

voltage across the sample, which increases the energy difference between the anode and the cathode, resulting in an increase in the potential and driving force in the cell. If there are any photocarriers, then, they will eventually be instigated to flow. If the photocurrent does not increase, then there are no photocarriers to stimulate and the material is not going to be active in that region. Such is the case with pure TiO_2 and the carbon doped samples show no improvement. Therefore even though the UV-vis and Kubelka Munk data suggest that the electronic structure is changing, it must not be sufficient to increase the photoactivity.

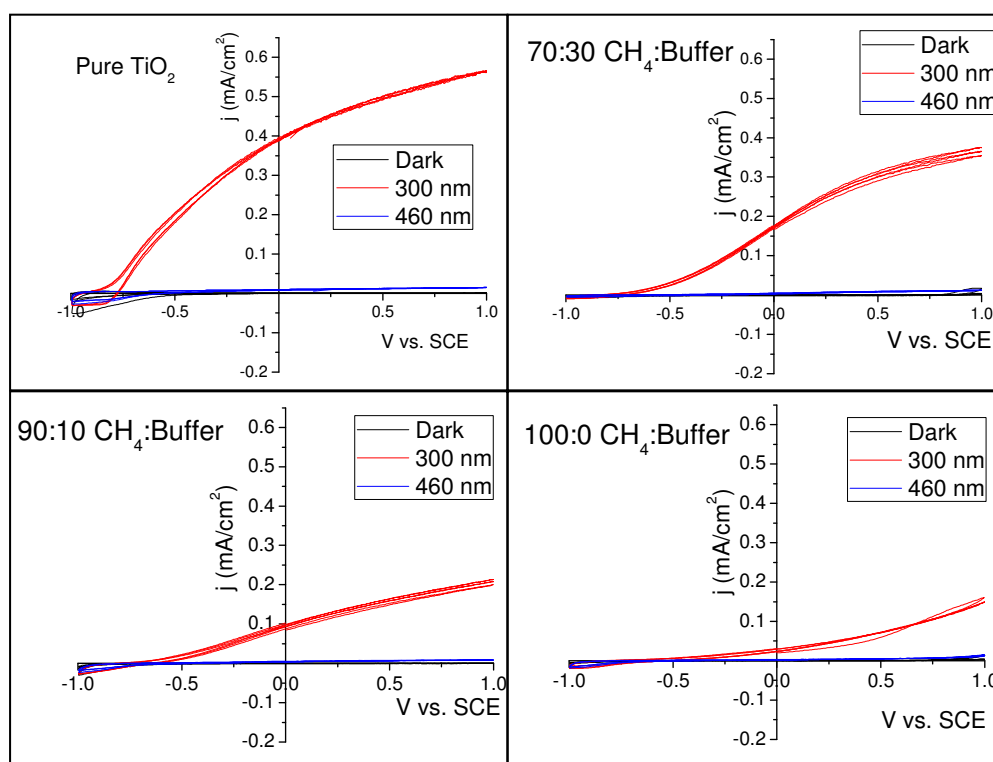


Figure 4.11 Selection of voltammetric data for pure TiO_2 and 70:30, 90:10, and 100:0 samples.

Since voltammetry is not calibrated for incoming radiation, however, it is not as rigorous a judge of efficiency as IPCE. Figure 4.12 shows the efficiency of the same samples as in Figure 4.11. None of the C-doped samples show efficiency improvements over pure TiO₂ in the UV or visible region; indeed, efficiency decreases with increasing carbon content. Therefore both the photocurrent and quantum efficiency do not increase with increasing carbon in the visible region as was the goal. Again, if there are doping states as previously suggested, they are probably not close enough to the valence band to effectively promote visible light catalysis.

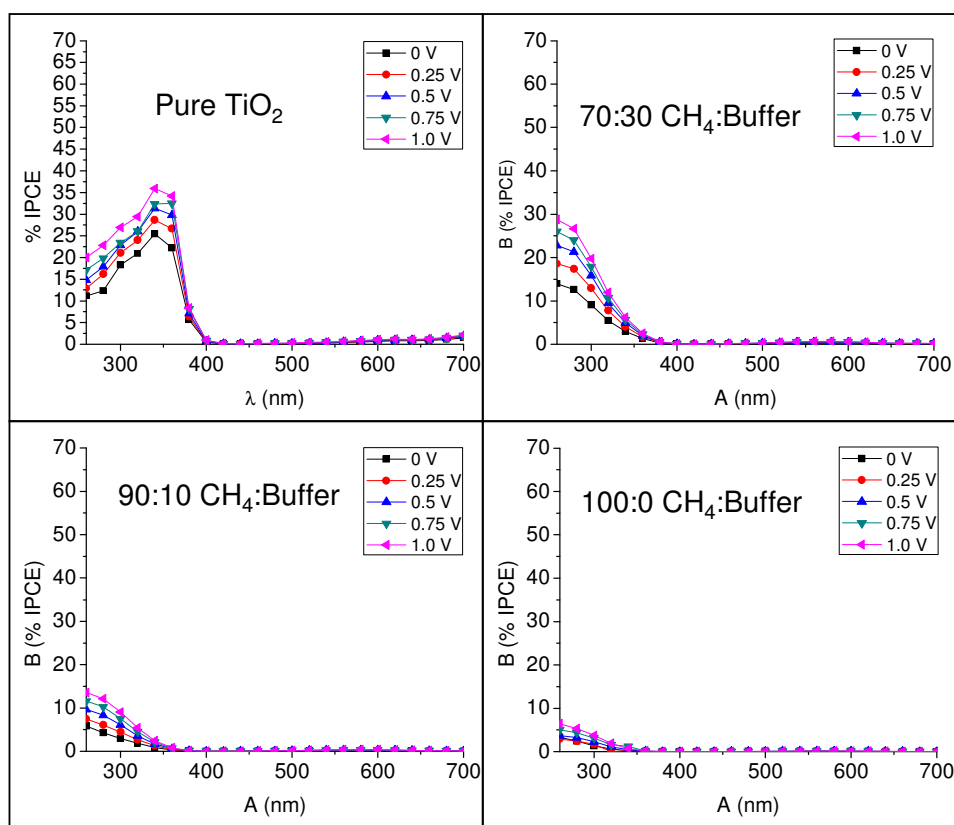


Figure 4.12 Selection of IPCE graphs for pure TiO₂ and 70:30, 90:10, and 100:0 samples.

Chapter 5

CONCLUSION

A slow evolution of investigation can be seen over the course of this research. Carbon dioxide trials were useful in that they helped establish a 1.6 cm substrate to target distance as optimal for crystallinity. As for actual lattice doping, however, they were not successful, as the oxygen content was too high. Methane was then used to obtain samples that showed crystallinity and characteristics associated with definite carbon doping. The films became darker and grain size and film thickness decreased with increased carbon concentration. A transformation from anatase to rutile was observed, showing a crystallinity change, and Kubelka-Munk calculations showed a red shift in the band gap, denoting an electronic change. Voltammetry and IPCE measurements show that even if carbon states have deposited and formed in the band gap, however, they have not increased the visible light reactivity or the efficiency of the films. Analysis of the carbon-doped films therefore shows only limited success.

Comparing these results to what is known from Asahi *et al.* (2001) in Figure 1.5 and from XPS analysis of the samples by another student, the development of intermediate stages is plausible. Carbon doping does not quite add on squarely to the oxygen 2s state. It is known that nitrogen doping is closer to the bottom TiO₂ edge, however, and that it can add on and decrease the band gap. It follows, then, that combining nitrogen and carbon doping may be the most beneficial avenue for this type of project. The potential overlap of carbon and nitrogen states is hypothesized to

narrow the band gap further, eliminate interstitial states, and allow successful charge transfer and visible light activity. If nothing else, the nitrogen and carbon doping research leading to this point can serve to recommend a codoping trial in this field in the future.

In conclusion, 630.8 billion cubic meters (52.6 million metric tons) of hydrogen were consumed worldwide in 2006, and approximately 96% of that was produced using fossil fuels.²⁰ Given this information, it can be seen that the industry stands to significantly reduce emissions and dependence on foreign fuels if solar-powered hydrogen generation becomes viable. Despite the advantages of TiO₂ as a cheap, available, and stable photocatalyst, its low efficiency still prevents wide application of the material as a photoanode for solar hydrogen generation. Since the latter is one of the technologies able to make hydrogen fuel cells truly emissions-free on both the consumer *and* industry level, it will be increasingly necessary to develop as hydrogen fuel cell cars come into production.

REFERENCES

Cited Works

- ¹ Lloyd, A and Cackette, T. “Diesel Engines: Environmental Impact and Control.” *Journal of Air and Waste Management Assoc.* **51** (2001) 809-847.
- ² “Cushing, OK WTI Spot Price FOB (Dollars per Barrel)” *U.S. Energy Information Administration*, April 1, 2009.
<<http://tonto.eia.doe.gov/dnav/pet/hist/rwtcd.htm>>
- ³ “Hydrogen Production Overview” Fact Sheet Series, The National Hydrogen Association and U.S. Department of Energy, Energy Efficiency and Renewable Energy sector. August 2004. www.HydrogenAssociation.org and
<www.eere.energy.gov/hydrogenandfuelcells/>
- ⁴ “Hydrogen Fact Sheet: Hydrogen Production – Steam Methane Reforming (SMR).” New York State Energy Research and Development Authority, www.nyseda.org.<www.getenergysmart.org/Files/HydrogenEducation/6HydrogenProductionSteamMethaneReforming.pdf>
- ⁵ T. Bak et al., “Photo-electrochemical hydrogen generation from water using solar energy.” *International Journal of Hydrogen Energy*, **27** (2002) 991 – 1022.
- ⁶ Fujishima, A; Rao, T; Tryk, D. “Titanium dioxide photocatalysis.” *Journal of Photochemistry and Photobiology C: Photochemistry Reviews*, **1** (2000) 1-21.
- ⁷ Sakthivel, S and Kisch, H. “Daylight Photocatalysis by Carbon-Modified Titanium Dioxide.” *Angew. Chem. Int. Ed.* **42**, (2003) 4908-4911.
- ⁸ Joe Smyth, “TiO₂ Structures.” University of Colorado, 2008.
<<http://ruby.colorado.edu/~smyth/min/tio2.html>>
- ⁹ Christiana Honsberg and Stuart Bowden. “Standard Solar Spectra.” NSF-Sponsored Photovoltaics CD-ROM, 2008.
<http://pvcrom.pveducation.org/APPEND/Am1_5.htm>

-
- 10 Lin, H., Schulz, M., Huang, C.P., Shah, S.I., "Synthesis of Visible Light Sensitive N-doped TiO₂ by Direct Oxidation of TiN", National Society of Vacuum Coaters (SVC) Annual Technical Conference, Chicago, IL, April 2008.
- 11 Huang, Y.; Ho, W.; Lee, S.; Zhang, L.; Li, G.; Yu, J. "Effect of Carbon Doping on the Mesoporous Structure of Nanocrystalline Titanium Dioxide and Its Solar-Light-Driven Photocatalytic Degradation of NO_x." *American Chemical Society*, 2008. DOI: 10.1021/la703333z
- 12 Lin, H.; Rumaiz, A.; Schulz, M.; Wang, D.; Rock, R.; Huang, C.; Shah, I.S.. "Photocatalytic activity of pulsed laser deposited TiO₂ thin films." *Materials Science and Engineering B*, 151 (2008) 133-139.
- 13 Lin, H.; Huang, C.; Li, W.; Ni, C.; Shah, S. I.; Tseng, Y-H. "Size dependency of nanocrystalline TiO₂ on its optical property and photocatalytic reactivity exemplified by 2-chlorophenol." *Applied Catalysis B: Environmental*, 68 (2006) 1-11.
- 14 Kortum, Gustav. *Reflectance Spectroscopy: Principles, Methods, Applications*, Springer-Verlag, 1969.
- 15 Chandra, Suresh. *Photoelectrochemical Solar Cells*, Electrocomponent Science Monographs, Volume 5, Gordon and Breach Science Publishers, Series Editor: D.S. Campbell. Copyright 1985.
- 16 Park, J.; Kim, S.; Bard, A. "Novel Carbon-Doped TiO₂ Nanotube Arrays with High Aspect Ratios for Efficient Solar Water Splitting." *Nano Letters*, Vol. 6, No. 1, 24-28, 2006.
- 17 Khan, S.; Al-Shahry, M.; Ingler Jr., W.; "Efficient Photochemical Water Splitting by a Chemically Modified n-TiO₂." *Science*, **297**, 2243 (2002); DOI: 10.1126/science.1075035.
- 18 Enache, C; Schoonman, J.; Van De Krol, R. "The Photoresponse of Iron- and Carbon-Doped TiO₂ (Anatase) Photoelectrodes." *Journal of Electroceramics*, 13, 177-182, 2004.

-
- 19 Norman, R.; Bonnett, R.; Coxon, J. *Principles of Organic Synthesis*. CRC Press, Nelson Thornes, Edition 3, 1993, ISBN: 0748761624, 9780748761623. p. 8. <<http://books.google.com/books?id=irNujn8i7rsC>>
- 20 “Study: Refineries’ Hydrogen Consumption Will Climb 40% in Next 5 Years.” *Green Car Congress*, 30 October, 2007. <<http://www.greencarcongress.com/2007/10/study-refinerie.html>>.

Additional References

- Reddy, K.; Baruwati, B.; Jayalakshimi, M.; Rao, M.; Manorama, S. “S-, N- and C-doped titanium dioxide nanoparticles: Synthesis, characterization and redox charge transfer study.” *Journal of Solid State Chemistry*, **178** (2005) 3352–3358.
- Mohapatra, S.; Misra, M.; Mahajan, V.; Raja, K. “Design of a Highly Efficient Photoelectrolytic Cell for Hydrogen Generation by Water Splitting: Application of TiO₂-xCx Nanotubes as a Photoanode and Pt/TiO₂ Nanotubes as a Cathode.” *J. Phys. Chem. C*, **111** (2007) 8677-8685.
- Raja, K.; Misra, M.; Mahajan, V.; Gandhi, T.; Pillai, P.; Mohapatra, S. “Photo-electrochemical hydrogen generation using band-gap modified nanotubular titanium oxide in solar light.” *Journal of Power Sources*, **161** (2006) 1450–1457